Structural basis of fatty acid activation and transport by human FATP2

Ao Li[1,2,3,4,5#], Junhui Shi[1,3,4,5#], Dan Ma[1,3,4,5]

[1]State Key Laboratory of Gene Expression, School of Life Sciences, Westlake University, Hangzhou, Zhejiang, China.

[2]Department of Landscape and Horticulture, Ecology College, Lishui University, Lishui 323000, Zhejiang, China.

[3]Key Laboratory of Structural Biology of Zhejiang Province, School of Life Sciences, Westlake University, Hangzhou, Zhejiang, China.

[4]Westlake Laboratory of Life Sciences and Biomedicine, Hangzhou, Zhejiang, China.

[5]Institute of Biology, Westlake Institute for Advanced Study, Hangzhou, Zhejiang, China.

These authors contributed equally: Ao Li and Junhui Shi

email: madan@westlake.edu.cn

Key Words: fatty acid, transport, FATP, membrane protein, drug target, LCFA, VLCFA, acyl-CoA synthetase, lipid metabolism, β-oxidation

Abstract

Fatty acids (FAs) are essential biomolecules that play critical roles in development and growth[1-4]. Fatty acid transport proteins (FATPs) are responsible for the transport of long-chain FAs (LCFAs) and very-long-chain FAs (VLCFAs), exhibiting bifunctionality that includes both FA transport and acyl-CoA synthetase activity. FATPs are potential drug targets for treating various metabolism-related diseases, including cancers[5-7]. However, the lack of three-dimensional structures of FATPs has hindered our understanding of their mechanisms. Here, we report a cryo-EM structure of human FATP2 in complex with an acyl-AMP intermediate and an incoming FA substrate at 2.9 Å resolution. The FA substrate, adopting a crescent shape, interacts with the membrane and a reclining membrane-associated helix of FATP2, with its tail half inserted into the membrane and its head half bound to a hydrophobic pocket on FATP2 at the protein-membrane interface. The acyl-AMP

is bound below the FA substrate, with the AMP portion in a large central pocket and the acyl group in a hydrophobic tunnel that connects the FA entry pocket and the central pocket. This structure reveals that the FA substrate from the membrane may undergo a two-step translocation process to access the catalytic center. The spacious inner cavity allows the binding of a new FA substrate before the completion of a full reaction cycle, which may be a crucial mechanism to ensure the catalytic and transport efficiency of FATP2. We also demonstrate that FATP2 transport FAs, strictly dependent on the activation of FAs through the acyl-CoA synthetase activity of FATP2. Our findings provide important insights into the catalytic and transport mechanisms of FATPs and offer a structural basis for the development of inhibitors targeting FATPs to treat related diseases.

Introduction

Fatty acids (FAs) play important roles in development and growth, primarily through their involvement in membrane biogenesis, energy metabolism, and cell signaling[1-4]. FAs can be classified according to their aliphatic chain length into short-chain (2–6 carbon atoms), medium-chain (8–12 carbon atoms), long-chain (14–18 carbon atoms), and very-long-chain (20–26 carbon atoms) FAs. In the circulation and tissues of mammals, FAs predominantly bear long and very long chains[8]. FAs are indispensable for numerous biological processes, including ATP generation via β-oxidation, the synthesis of structural lipids such as phospholipids and sphingolipids, and the synthesis of signaling molecules like eicosanoid[1-4,9]. Typically, FA molecules are activated by linking to Coenzyme A (CoA) to form acyl-CoA, a necessary intermediate for FA elongation, β-oxidation, phospholipid generation, and the synthesis of neutral lipids such as triacylglycerol (TAG)[10]. Furthermore, fatty acids may directly or indirectly interact with membranes, ion channels, transporters, hormone receptors, and enzymes, influencing various cellular functions[11].

Fatty acid transport proteins (FATPs) constitute a family of conserved membrane-bound proteins responsible for the transport of long-chain fatty acids (LCFAs) and very-long-chain fatty acids (VLCFAs), which are limited in passive diffusion[12-14]. FA transport activity and

ATP-dependent acyl-CoA synthetase activity for FA activation have been demonstrated in FATPs[15-21]. Six members of FATPs (FATP1-6) in humans exhibit distinct patterns in tissue distribution, expression, and subcellular localization, and are crucial for fatty acid uptake and utilization, as well as lipid homeostasis in corresponding tissues and cells[22]. Fatty acid uptake and metabolism are essential for cellular metabolic networks, particularly lipid metabolism, and an imbalance in lipid flux can remodel or impair cell metabolism, leading to a variety of human diseases, including cancers and heart failure[5-7,23,24]. FATPs are important drug targets for the treatment of related diseases. Despite their importance, three-dimensional structures of these FA transport proteins are lacking, hindering a deeper understanding of their working mechanisms.

Here, we report a cryo-EM structure of human FATP2 bound to an incoming FA substrate and an acyl-AMP at 2.9 Å resolution, representing an intermediate state during FA activation and transport by FATP2. Our results provide a structural basis for understanding the mechanisms of acyl-CoA generation and FA transport by FATPs.

Results

Overall structure of FATP2

FATP2 bears both acyl-CoA synthetase activity and fatty acid transport activity (Fig. 1a). To elucidate the working mechanism of FATP2 and understand the relationship between the two functions, we performed structural studies and biochemical analysis towards FATP2.

Human FATP2 was recombinantly expressed in HEK293F cells and purified into homogeneity for cryo-EM analysis. Following data acquisition and processing, a cryo-EM map at 2.9 Å resolution was obtained, enabling structural model building.

In the cryo-EM structure, we observed FATP2 bound to both an acyl-AMP intermediate and an incoming fatty acid substrate (Fig. 1b). FATP2 is composed of four domains: the membrane association domain (MAD), the cytosolic N-terminal domain (NTD), the core catalytic domain (CCD), and the C-terminal domain (CTD) (Fig. 1b). The cytosolic regions of

FATP2 form an arch-like structure, with the NTD and CTD situated on opposite sides of the CCD. The MAD comprises an N-terminal transmembrane helix (TM), of which only the C-half is modeled based on the density, and a subsequent reclining helix (RH) attached to the membrane. MAD serves as an anchor, fixing FATP2 to the membrane. Both the NTD and CTD are similarly arranged into β-α-β-α structures. The CCD domain exhibits a saddle-shaped structure, with two subdomains arranged side by side, accommodating the MAD-RH in the middle groove.

The FA is bound at the interface between the membrane and FATP2 (Fig. 1b, c). The tail-half interacts with the membrane and RH, while the head-half is inserted into a pocket on the top of CCD, referred to as the entry pocket (Fig. 1d). The acyl-AMP is located below the FA substrate, with the AMP portion accommodated by a large central pocket and the acyl group placed in a tunnel connecting the entry pocket and the central pocket (Fig. 1d). A cofactor magnesium ion (Mg^{2+}) is bound below the acyl-AMP in CCD (Fig. 1d), indicating that the reaction center for acyl-CoA synthetase activity is likely situated nearby. The FA, bound at the entry pocket, is distant from the Mg^{2+} and thus the reaction center, suggesting that translocation of the FA substrate must occur to gain access to the reaction center. Additionally, below the acyl-AMP, a large vertical channel faces the cytoplasm (Fig. 1e), which may allow the passage of other substrates and products.

The binding site of the FA substrate

Multiple views of the cryo-EM map of FATP2 suggest that the FA bound at the entry pocket has a crescent shape and wraps around RH in FATP2 (Fig. 2a, b), with the tail-half of FA inserted into the membrane side (Fig. 2a, c). It may represent the interaction mode between FAs and native membrane environment when FAs are initially captured and mounted onto FATP2. The head-half of FA binds into the hydrophobic entry pocket formed by hydrophobic residues from both RH and CCD at the membrane-protein interface (Fig. 1d, 2c). The hydrophobic tail of FA interacts with Tyr32, Phe33, Val36, Ala37, and Val39 in RH, and Tyr244, Leu248, Val251, Ile391, Ile392, and Leu432 in CCD. Additionally, a hydrogen

bond is formed between the carboxyl group of FA and the hydroxyl group of Tyr32 in RH, which may stabilize the binding of FA to FATP2 at the entry pocket.

During the ATP-dependent FA activation process, AMP is one of the final products during FATP2-mediated acyl-CoA formation (Fig. 1a). AMP production was measured by HPLC and peak area was used to represent the enzymatic activity of FATP2. We generated FATP2 mutants with alterations in the FA entry pocket and examined their effects on enzymatic activity. Compared to wild-type (WT) FATP2, AMP production decreased by approximately 50% in the Y32G mutant, which may disrupt the interaction between FA substrates and FATP2, and in the Y244W mutant, which may reduce the space at the entry pocket (Fig. 2d). These findings suggest that the initial binding of the FA substrate at the entry pocket is crucial for the catalytic activity of FATP2.

The binding sites of acyl-AMP and Mg^{2+}

In the FATP2 structure, the intermediate product acyl-AMP is primarily bound to CCD (Fig. 3a, b), with the AMP portion accommodated in the central pocket, and the acyl group positioned in the connection tunnel between the FA entry pocket and the central pocket (Fig. 1d). Extensive interactions are generated between the acyl-AMP and FATP2, and a magnesium ion is bound below the acyl-AMP (Fig. 3c), closed to the phosphate group in AMP. The acyl-AMP forms hydrogen bonds with side chains of His268, Ser269, Asn339, Glu360, Thr365, Asp465, Arg480 and Lys572, as well as with the main chains of Phe361, Ala363 and Thr365. The phosphate group of AMP engages in electrostatic interactions with Arg480 and Lys572, with Lys572 in CTD being the only residue from a different domain besides CCD. The hydrophobic acyl group of the acyl-AMP is placed in the tunnel connecting the FA entry pocket and the central pocket. This tunnel is primarily composed of hydrophobic residues, including Ile237, Ile242, Tyr244, Leu248, Ala270, Leu273, Ile274, Phe361, Tyr362, Ala363, Ala364, Ile369, Phe371, Ile392, Pro434 and Phe435. The Mg^{2+} is bound below the acyl-AMP, forming a hydrogen bond with the side chain of Thr225 and a

salt bridge with Glu366. The Mg^{2+} also interacts with the phosphate group of the acyl-AMP through electrostatic interaction.

To examine the importance of the residues at the binding sites of Mg^{2+} and the acyl-AMP, we introduced mutations and compared corresponding AMP production of the mutants to that of WT FATP2 (Fig. 3d). The AMP production of both Mg^{2+} binding site mutants, carrying the T225A or E366A mutations, was significantly decreased, with the E366A mutant exhibiting a reduction of more than 70%. We also measured the enzymatic activity of FATP2 variants bearing mutations in residues involved in polar interactions with the acyl-AMP. The results suggested that all mutants carrying the H268A, N339A, R480A and K572A mutations exhibited reduced enzymatic activity of FATP2, with the H268A and K572A mutants showing the most dramatic decreases in AMP production, by more than 70% and 95%, respectively. Besides generating electrostatic interactions with the phosphate group in the acyl-AMP, both His268 and Lys572 form hydrogen bonds with the same hydroxyl oxygen of the phosphate group, while Lys572 also forms additional hydrogen bonds with two oxygens from the ribose ring and the carbonyl group of the acyl moiety (Fig. 3e). It seems that Lys572 may be important to the binding of intermediate product acyl-AMP and is essential for the catalysis. Interestingly, the mutant carrying the T365A mutation increased FATP2-mediated AMP production by more than 50% (Fig. 3d). Since Thr365 is observed to form hydrogen bonds with the other free hydroxyl group of the AMP phosphate group and the ester linkage of the acyl-AMP (Fig. 3e), we speculate that the mutation of Thr365 may facilitate the access of the acceptor group for the acyl moiety in CoA to the ester linkage and/or enhance the rate of product release during the reaction.

Fatty acid transport by FATP2

To examine FA transport activity of FATP2, we performed a proteoliposome-based transport assay (Fig. 4a). C1-BODIPY-C12, a fluorescence-labeled fatty acid derivative widely used to monitor fatty acid uptake[15,25,26], was incorporated into the lipid bilayer during liposome preparation and serves as the FA substrates for FATP2. Other substrates and co-

factors were added to the outside assay buffer to initiate FA transport towards the external environment, and the resulting external fluorescence was recorded after the removal of the liposomes.

Transport assay results suggested that WT FATP2 efficiently transported FA substrates to outside when Mg^{2+}, ATP, and CoA were supplemented; however, almost no substrate transport was detected in the absence of CoA (Fig. 4b). We also evaluated FA transport by the K572A mutant, which reduced enzymatic activity by more than 95% (Fig. 3d), and found that the substrate transport by this mutant was also decreased by more than 90% (Fig. 4b). These findings suggest that FATP2-mediated FA transport is strictly dependent on its acyl-CoA synthetase activity.

Discussion

Based on our structural findings and biochemical analysis, we propose a working model for FATP2 during one FA transport cycle dependent on FA activation (Fig. 4c): A FA substrate absorbed by membrane from the extracellular matrix is first captured by FATP2 followed by initial mounting at the entry pocket, and the FA substrate will be subsequently translocated to the catalytic center, where Mg^{2+} and ATP are bound to generate acyl-AMP. CoA will bind to FATP2, though the binding details are unclear due to the difficulties in obtaining the atomic 3D structure, with its thiol group gaining access to the reaction center to accept the acyl group from acyl-AMP. The final products AMP and acyl-CoA will be generated after the transfer of acyl group from acyl-AMP to CoA. Fatty acids are transported into the cytoplasm by FATP2 in the form of acyl-CoA. During the catalysis-dependent FA transport process, substrates and products may be exchanged through the bottom, cytoplasm-facing channel, which is ideal in size and location. A new FA substrate from the membrane can bind to the entry pocket as long as there is a vacancy, regardless of the stage of the reactions. Catalysis-coupled FA transport cycles mediated by FATP2 may provide the driving force for the incorporation of FAs into the membrane, which may further provide substrates for FATP2, and thus enhance FA uptake.

The primary sequences are conserved among all six human FATPs and among FATP2s across species (Supplementary Figs. 1,2). Residues in the reaction center involved in binding with Mg^{2+} and the AMP portion of acyl-AMP, as well as those forming the bottom channel possible for substrate/product passage, are highly conserved. Interestingly, residues involved in binding with the FA substrate and the acyl group of acyl-AMP, although similar in hydrophobic properties, are less conserved. This may result in variable preferences for FA substrates among FATPs. Structural comparisons between our cryo-EM structure of FATP2 and AlphaFold-predicted structures of other human FATPs suggest that all six FATPs are structurally conserved in the cytosolic regions (Supplementary Fig. 3). Therefore, other FATPs may share similar mechanisms for catalysis and FA transport.

Taken together, our studies reveal structural features of FATP2 and its binding modes with a FA substrate and an acyl-AMP intermediate product, facilitating the identification of a conserved catalytic site and other important structural elements. These findings offer crucial insights into the activation and transport mechanisms of FA by FATP2, which also enhance our understanding of the molecular mechanisms of other FATP family members. This study also provides a structural foundation for the development of inhibitors targeting FATP-mediated FA activation and transport, with potential applications in the treatment of related human diseases, including cancers.

Methods

Protein expression and purification

Human FATP2 (UniProt ID: O14975) variants were cloned into pCAG vector with an N-terminal Flag-tag. Plasmids were transiently transfected into HEK293F cells at density of 2.0 × 10^6 cells/ml and cultured in SMM 293-TII medium (Sino Biological) at 37 °C under 5% CO2. After 60 h, cells were harvested and resuspended in the buffer containing 25 mM HEPES pH 7.4, 150 mM NaCl, 5 μg/ml aprotinin, 1 μg/ml pepstatin, 5 μg/ml leupeptin and 1 mM PMSF. Cell membrane was solubilized with 1% (w/v) n-dodecyl-β-D-maltoside (DDM, Anatrace) at 4 °C for 2 h. After high-speed centrifugation at 25,000 g for 1 h, the supernatant was loaded onto anti-Flag resin (GenScript). Then the resin was washed with buffer containing 25 mM

HEPES pH 7.4, 150 mM NaCl, and 0.03% (w/v) DDM. Proteins were eluted with wash buffer supplemented with FLAG peptide at 0.2 mg/ml concentration.

The membrane scaffold protein MSP1D1 bearing N-terminal His-tag for nanodisc reconstitution was expressed in *E. coli* BL21(DE3) cells. Collected cells were lysed by sonication in lysis buffer (20 mM sodium phosphate buffer, pH 7.4) supplemented with 1 mM PMSF and 1% Triton X-100. After centrifugation at 30,000 g for 30 min at 4 °C, the supernatant was loaded onto the nickel-affinity resin. The resin was washed with 40 mM Tris/HCl pH 8.0, 300 mM NaCl, 5 mM sodium cholate and 30 mM imidazole. Protein was eluted with elution buffer containing 10 mM Tris/HCl pH 7.4, 100 mM NaCl, 5 mM sodium cholate and 300 mM imidazole. The elution was concentrated and loaded onto a Superdex 200 Increase column for further purification. The MSP1D1-containing fractions were pooled for nanodisc reconstitution.

Reconstitution of FATP2 into lipid nanodiscs

1-palmitoyl-2-oleoyl-sn-glycero-3-phospho-(1'-rac)-choline (POPC, Avanti Polar Lipids) and 1-palmitoyl-2-oleoyl-sn-glycero-3-phospho-(1′-rac-glycerol) (sodium salt) (POPG, Avanti Polar Lipids) were solubilized in chloroform at 1:3 molar ratio. Above solution was dried under nitrogen gas and resuspended with buffer containing 2.5 mM cholesteryl hemisuccinate tris salt (CHS, Anatrace) and 30 mM DDM. FATP2, MSP1D1 and lipid mixture were mixed at a molar ratio of 1:5:60 and incubated at 4 °C for 30 min. Detergents were removed by incubation with Bio-beads SM2 (Bio-Rad) overnight at 4 °C. The protein-lipid mixture was loaded onto a size-exclusion column equilibrated with 25 mM HEPES pH 7.4 and 150 mM NaCl. The purified nanodiscs were collected for cryo-EM sample preparation.

Cryo-EM sample preparation and data collection

The FATP2 reconstituted into nanodiscs was loaded onto grid followed by a 3.5 s blotting using Vitrobot Mark IV (ThermoFisher Scientific). After blotting, grids were rapidly immersed into pre-cooled liquid ethane and transferred to liquid nitrogen. Image acquisitions were performed on Titan Krios G4 (FEI) operating at 300 kV with a Selectris X imaging filter

(Thermo Fisher Scientific) and Falcon 4i direct electron detector (Thermo Fisher Scientific). Data were collected in counted super-resolution mode at magnification of 215,000 x, physical pixel size of 0.57 Å. Movie stacks were automatically acquired using Thermo Scientific EPU (Thermo Fisher Scientific) with a 20 eV slit width and a defocus range from −0.9 to − 1.5 µm. The movies were stored as EER format which were exposed for 2.45 s with total dose of ~50 e^{-}/Å².

Cryo-EM data processing

Motion-correction and dose weighting were performed using Patch Motion Correction in cryoSPARC[27]. Contrast transfer function (CTF) parameters were estimated with Patch-CTF in cryoSPARC. Micrographs with CTF fitting resolution worse than 6 Å were excluded during manual curation. Initial particles were picked from few partial micrographs using blob picker in cryoSPARC and 2D averages were generated. Final particle picking was done by template picker using templates from those 2D results. 4313 k particles were extracted from 14265 micrographs with pixel size of 9.12 Å (box size 30 pixels), After one round of 2D classification, the good particles were re-extracted and re-centered with pixel size of 4.56 Å (box size 60 pixels) for the next 2D classification. Above process was continued until the particles were re-extracted with pixel size of 1.14 Å (box size 240 pixels). After 4 rounds of 2D classification to remove obvious junk, a total of 129 k particles were retained. This data set was then used for ab-initio reconstruction, with carefully tuning parameters including the number of classes, initial resolution, initial and final minibatch sizes using cryoSPARC. A resulting map with better secondary structural features was generated from a 3 classes ab-initio reconstruction. After non-uniform (NU) refinement[28], a good reference at 4.27 Å resolution was generated for the next 3D classification.

Another 12952 micrographs were combined with above 14265 micrographs, from which a total of 7307 k particles were extracted with pixel size of 9.12 Å (box size 30 pixels). These particles were subjected to 4 rounds of 2D classification and 275 k particles with pixel size of 1.14 Å were remained. The map at 4.27 Å resolution was used as a good reference for the hetero refinement of the 275 k particles. After hetero refinement and NU-refinement, a map

with a resolution of 3.54 Å was reconstructed using 137 k particles. To further improve the resolution, seed-facilitated 3D classification[29] was performed. A dataset as the seed pool, containing 1929 k particles was re-extracted with pixel size of 0.57 Å (box size 480 pixels). The above 137 k particles were also re-extracted with pixel size of 0.57 Å (box size 480 pixels) and used as seeds for seed-facilitated 3D classification. After 3 rounds of seed-facilitated 3D classification, 469 k particles were subjected to NU-refinement, which resulted in map with a resolution of 3.13 Å. After hetero refinement, ab-initio reconstruction and NU-refinement, a final map at an average resolution of 2.93 Å was reconstructed by 143 k particles.

Model building and refinement

The initial structure model for FATP2 was generated by AlphaFold2[30]. The structure was docked into the density map and manually adjusted and re-built by COOT[31]. Model refinement was performed using phenix.real_space_refine in PHENIX[32]. For cross-validations, the model vs. map Fourier Shell Correlation (FSC) curves were generated in the Comprehensive Validation module in PHENIX. The structure was validated through examination of the Molprobity scores[33], and statistics of the Ramachandran plots. Local resolutions were estimated using cyroSPARC1 local resolution estimation. Structural Figures were generated using PyMOL[34], UCSF Chimera[35] and ChimeraX[36].

Acyl-CoA synthetase activity assay

Enzyme activity was measured by AMP production through HPLC (Dionex Ultimate 3000 UHPLC+) at wavelength of 259 nm. Reactions were performed in buffers containing 150 mM NaCl, 1 mM $MgCl_2$, 2.5 mg/mL cyclodextrin, with 200 μM CoA, 1 mM ATP, and 500 μM oleic acid, and 25 mM various choices of pH buffer. Reactions were terminated by the supplementation of chloroform. Additional chloroform extraction was performed to remove proteins and lipids. Each resulting aqueous sample was mixed with an equal volume of 5% perchloric acid and then run isocratically with a mobile phase (100 mM sodium acetate, 75 mM monosodium phosphate, pH 4.6) on a C18 column (Thermo fisher BDS Hypersil).

Preparation of liposomes and proteoliposomes

Air-dried POPC and POPG solution (POPC: POPG at 1:3 molar ratio in chloroform) was resuspended to 20 mg/ml with buffer containing 25 mM HEPES pH 7.4, 150 mM NaCl and 40 μM C1-BODIPY-C12. Protein-free liposomes were obtained by extrusion. Then 1% n-octyl-β-D-glucopyranoside (β-OG, Anatrace) was supplemented before final 150 μg/ml FATP2 was added for 2~3 h incubation at 4 °C. Detergents were removed by Bio-Beads SM2. Resulting proteoliposomes were harvested by ultracentrifugation at 75,500 g for 30 min, following with wash and ultracentrifugation for another four times to remove free C1-BODIPY-C12 and proteins. The pellets were resuspended to 100 mg/ml with HEPES buffer for FA transport assay.

FA transport assay

FA transport assays were performed by adding 25 μl proteoliposomes into 75 μl assay buffer containing 25 mM HEPES pH 7.4, 150 mM NaCl, 1 mM $MgCl_2$, 1 mM ATP and 0.3 mM CoA. After incubation for 2 min at 37 °C. The reaction was terminated with 900 μl ice-cold sodium acetate buffer (100 mM sodium acetate pH 4.5, 150 mM NaCl). After centrifugation at 75,500 g for 30 min, the supernatant was collected for measurement of the fluorescence intensity at excitation wavelength of 475 nm and emission wavelength of 516 nm.

Data availability

Data supporting the findings of this manuscript are available from the corresponding author upon reasonable request. The atomic coordinate and corresponding EM map of FATP2 have been deposited in the Protein Data Bank (http://www.rcsb.org) with PDB ID 9VZP and the Electron Microscopy Data Bank (https://www.ebi.ac.uk/pdbe/emdb/) with EMDB ID EMD-65482, respectively.

Reference

1 Houten, S. M., Violante, S., Ventura, F. V. & Wanders, R. J. The Biochemistry and Physiology of Mitochondrial Fatty Acid β-Oxidation and Its Genetic Disorders. *Annu Rev Physiol* **78**, 23-44, doi:10.1146/annurev-physiol-021115-105045 (2016).

2 Nohturfft, A. & Zhang, S. C. Coordination of lipid metabolism in membrane biogenesis. *Annu Rev Cell Dev Biol* **25**, 539-566, doi:10.1146/annurev.cellbio.24.110707.175344 (2009).

3 Zadoorian, A., Du, X. & Yang, H. Lipid droplet biogenesis and functions in health and disease. *Nat Rev Endocrinol* **19**, 443-459, doi:10.1038/s41574-023-00845-0 (2023).

4 Brennan, E., Kantharidis, P., Cooper, M. E. & Godson, C. Pro-resolving lipid mediators: regulators of inflammation, metabolism and kidney function. *Nat Rev Nephrol* **17**, 725-739, doi:10.1038/s41581-021-00454-y (2021).

5 Veglia, F. *et al.* Fatty acid transport protein 2 reprograms neutrophils in cancer. *Nature* **569**, 73-78, doi:10.1038/s41586-019-1118-2 (2019).

6 Glatz, J. F., Luiken, J. J. & Bonen, A. Membrane fatty acid transporters as regulators of lipid metabolism: implications for metabolic disease. *Physiol Rev* **90**, 367-417, doi:10.1152/physrev.00003.2009 (2010).

7 Hagberg, C. E. *et al.* Vascular endothelial growth factor B controls endothelial fatty acid uptake. *Nature* **464**, 917-921, doi:10.1038/nature08945 (2010).

8 Samovski, D., Jacome-Sosa, M. & Abumrad, N. A. Fatty Acid Transport and Signaling: Mechanisms and Physiological Implications. *Annu Rev Physiol* **85**, 317-337, doi:10.1146/annurev-physiol-032122-030352 (2023).

9 Spector, A. A. & Yorek, M. A. Membrane lipid composition and cellular function. *J Lipid Res* **26**, 1015-1035 (1985).

10 Grevengoed, T. J., Klett, E. L. & Coleman, R. A. Acyl-CoA metabolism and partitioning. *Annu Rev Nutr* **34**, 1-30, doi:10.1146/annurev-nutr-071813-105541 (2014).

11 Dutta-Roy, A. K. Cellular uptake of long-chain fatty acids: role of membrane-associated fatty-acid-binding/transport proteins. *Cell Mol Life Sci* **57**, 1360-1372, doi:10.1007/pl00000621 (2000).

12 Snaebjornsson, M. T., Janaki-Raman, S. & Schulze, A. Greasing the Wheels of the Cancer Machine: The Role of Lipid Metabolism in Cancer. *Cell Metab* **31**, 62-76, doi:10.1016/j.cmet.2019.11.010 (2020).

13 Kleinfeld, A. M., Chu, P. & Romero, C. Transport of long-chain native fatty acids across lipid bilayer membranes indicates that transbilayer flip-flop is rate limiting. *Biochemistry* **36**, 14146-14158, doi:10.1021/bi971440e (1997).

14 Hirsch, D., Stahl, A. & Lodish, H. F. A family of fatty acid transporters conserved from mycobacterium to man. *Proc Natl Acad Sci U S A* **95**, 8625-8629, doi:10.1073/pnas.95.15.8625 (1998).

15 Stahl, A. *et al.* Identification of the major intestinal fatty acid transport protein. *Mol Cell* **4**, 299-308, doi:10.1016/s1097-2765(00)80332-9 (1999).

16 Gimeno, R. E. *et al.* Targeted deletion of fatty acid transport protein-4 results in early embryonic lethality. *J Biol Chem* **278**, 49512-49516, doi:10.1074/jbc.M309759200 (2003).

17 Schaffer, J. E. & Lodish, H. F. Expression cloning and characterization of a novel adipocyte long chain fatty acid transport protein. *Cell* **79**, 427-436, doi:10.1016/0092-8674(94)90252-6 (1994).

18 Black, P. N., Ahowesso, C., Montefusco, D., Saini, N. & DiRusso, C. C. Fatty Acid Transport Proteins: Targeting FATP2 as a Gatekeeper Involved in the Transport of Exogenous Fatty Acids. *Medchemcomm* **7**, 612-622, doi:10.1039/c6md00043f (2016).

19 Melton, E. M., Cerny, R. L., DiRusso, C. C. & Black, P. N. Overexpression of human fatty acid transport protein 2/very long chain acyl-CoA synthetase 1 (FATP2/Acsvl1) reveals distinct patterns of trafficking of exogenous fatty acids. *Biochem Biophys Res Commun* **440**, 743-748, doi:10.1016/j.bbrc.2013.09.137 (2013).

20 Coe, N. R., Smith, A. J., Frohnert, B. I., Watkins, P. A. & Bernlohr, D. A. The fatty acid transport protein (FATP1) is a very long chain acyl-CoA synthetase. *J Biol Chem* **274**, 36300-36304, doi:10.1074/jbc.274.51.36300 (1999).

21 Falcon, A. *et al.* FATP2 is a hepatic fatty acid transporter and peroxisomal very long-chain acyl-CoA synthetase. *Am J Physiol Endocrinol Metab* **299**, E384-393, doi:10.1152/ajpendo.00226.2010 (2010).

22 Anderson, C. M. & Stahl, A. SLC27 fatty acid transport proteins. *Mol Aspects Med* **34**, 516-528, doi:10.1016/j.mam.2012.07.010 (2013).

23 Schulze, P. C., Drosatos, K. & Goldberg, I. J. Lipid Use and Misuse by the Heart. *Circ Res* **118**, 1736-1751, doi:10.1161/circresaha.116.306842 (2016).

24 Michos, E. D., McEvoy, J. W. & Blumenthal, R. S. Lipid Management for the Prevention of Atherosclerotic Cardiovascular Disease. *N Engl J Med* **381**, 1557-1567, doi:10.1056/NEJMra1806939 (2019).

25 Stahl, A., Evans, J. G., Pattel, S., Hirsch, D. & Lodish, H. F. Insulin causes fatty acid transport protein translocation and enhanced fatty acid uptake in adipocytes. *Dev Cell* **2**, 477-488, doi:10.1016/s1534-5807(02)00143-0 (2002).

26 Kolahi, K., Louey, S., Varlamov, O. & Thornburg, K. Real-Time Tracking of BODIPY-C12 Long-Chain Fatty Acid in Human Term Placenta Reveals Unique Lipid Dynamics in Cytotrophoblast Cells. *PLoS One* **11**, e0153522, doi:10.1371/journal.pone.0153522 (2016).

27 Punjani, A., Rubinstein, J. L., Fleet, D. J. & Brubaker, M. A. cryoSPARC: algorithms for rapid unsupervised cryo-EM structure determination. *Nat Methods* **14**, 290-296, doi:10.1038/nmeth.4169 (2017).

28 Punjani, A., Zhang, H. & Fleet, D. J. Non-uniform refinement: adaptive regularization improves single-particle cryo-EM reconstruction. *Nat Methods* **17**, 1214-1221, doi:10.1038/s41592-020-00990-8 (2020).

29 Wang, N. *et al.* Structural basis of human monocarboxylate transporter 1 inhibition by anti-cancer drug candidates. *Cell* **184**, 370-383.e313, doi:10.1016/j.cell.2020.11.043 (2021).

30 Jumper, J. *et al.* Highly accurate protein structure prediction with AlphaFold. *Nature* **596**, 583-589, doi:10.1038/s41586-021-03819-2 (2021).

31 Emsley, P. & Cowtan, K. Coot: model-building tools for molecular graphics. *Acta Crystallogr D Biol Crystallogr* **60**, 2126-2132, doi:10.1107/s0907444904019158 (2004).

32 Afonine, P. V. *et al.* Real-space refinement in PHENIX for cryo-EM and crystallography. *Acta Crystallogr D Struct Biol* **74**, 531-544, doi:10.1107/s2059798318006551 (2018).

33 Davis, I. W. *et al.* MolProbity: all-atom contacts and structure validation for proteins and nucleic acids. *Nucleic Acids Res* **35**, W375-383, doi:10.1093/nar/gkm216 (2007).

34 DeLano, W. L. *The PyMOL Molecular Graphics System.*, <http://www.pymol.org> (2002).

35 Pettersen, E. F. *et al.* UCSF Chimera--a visualization system for exploratory research and analysis. *J Comput Chem* **25**, 1605-1612, doi:10.1002/jcc.20084 (2004).

36 Pettersen, E. F. *et al.* UCSF ChimeraX: Structure visualization for researchers, educators, and developers. *Protein Sci* **30**, 70-82, doi:10.1002/pro.3943 (2021).

Acknowledgements

We would like to thank the following facilities at Westlake University: Cryo-EM Facility for providing cryo-EM support, High-Performance Computing Center for computational resources and related assistance, and the Mass Spectrometry & Metabolomics Core Facility for sample analysis. This work was supported by the State Key Laboratory of Gene Expression (2025ZY01117), the National Key R&D Program (2022YFA1303700), the Zhejiang Key Laboratories Project (2024E10052) and Westlake Education Foundation.

Author Contributions

D.M. conceived the project and wrote the manuscript. D.M. supervised on and provided methodology to structural and functional studies. A.L. contributed to protein expression and purification, cryo-EM sample preparation, data collection, assay system set up and biochemical assays. J.S. contributed to cryo-EM data processing, model building, protein purification and related assays.

Ethics statement

Competing interests

The authors declare no competing interests.

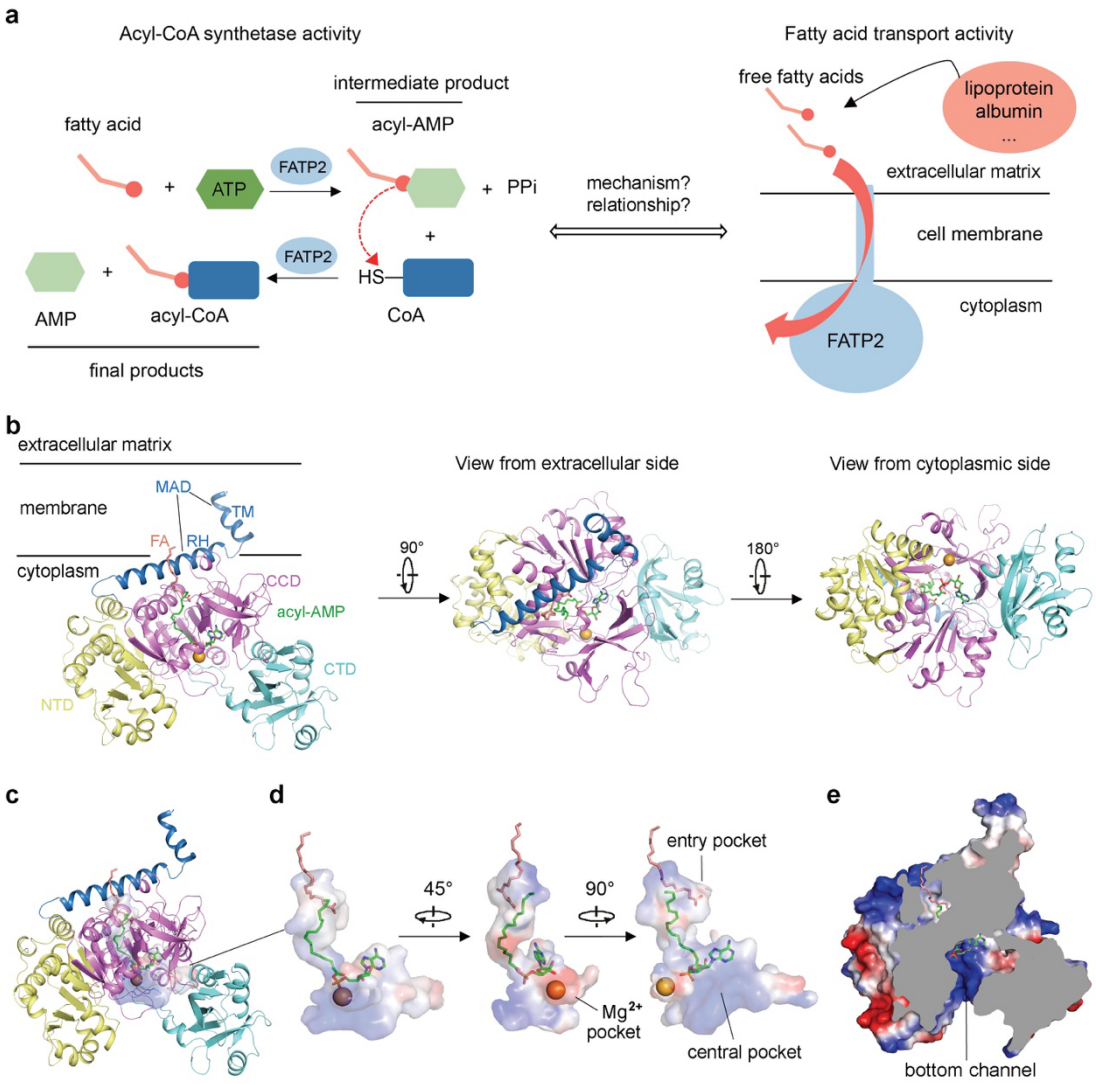

Fig. 1 Cryo-EM structure of FATP2 in complex with FA and acyl-AMP. a, An illustration of the acyl-CoA synthetase and fatty acid transport activities of FATP2. **b,** Overall structure of FATP2. The membrane association domain (MAD), cytosolic N-terminal domain (NTD), core catalytic domain (CCD), C-terminal domain (CTD), FA substrate, acyl-AMP intermediate product and magnesium ion are colored blue, yellow, violate, cyan, salmon, green and orange, respectively. **c,** The inner spaces for accommodation of FA, acyl-AMP and magnesium ion in FATP2 structure. Electrostatic surface was generated with only the culled cavities and pockets shown at 60% transparency. **d,** Different views of the continuous inner spaces with the entry pocket for FA, central pocket for acyl-AMP and the binding pocket for magnesium ion indicated. **e,** A cut-away surface of the FATP2 structure. The large bottom cytoplasm-facing channel is indicated.

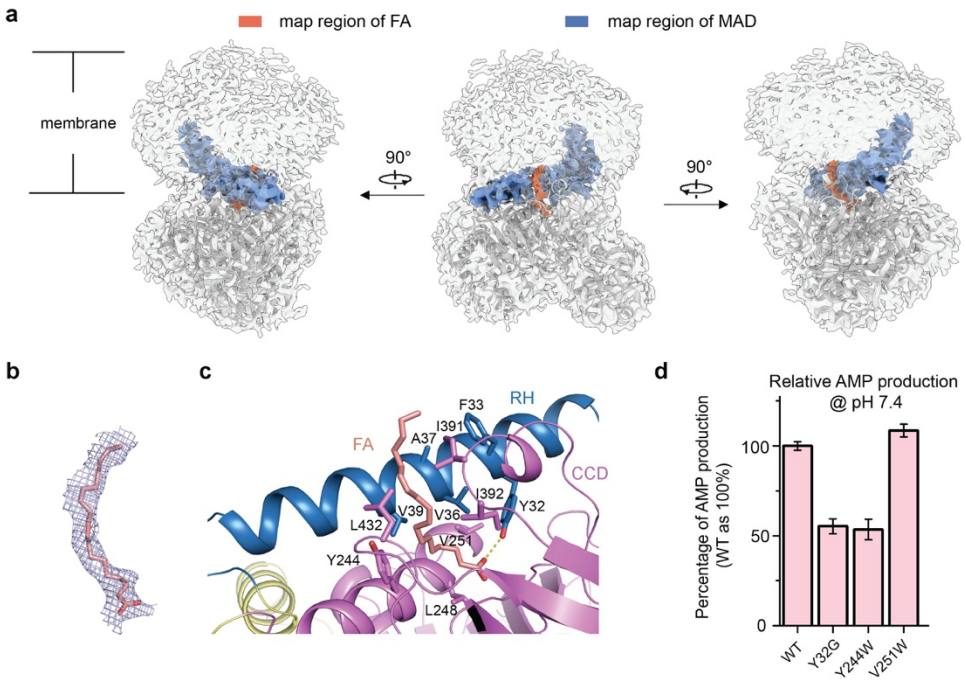

Fig. 2 The FA substrate binding site. a, Different views of FA binding in the cryo-EM map. Map regions of the FA and MAD are highlighted. **b,** The cryo-EM density of the FA. **c,** The binding details between the FA and FATP2. **d,** Relative acyl-CoA synthetase activity of FA binding site mutants compared to that of WT FATP2. AMP production of WT FATP2 was taken as 100%. All enzymatic assay data are shown as mean ± s.d., n = 3 technical replicates.

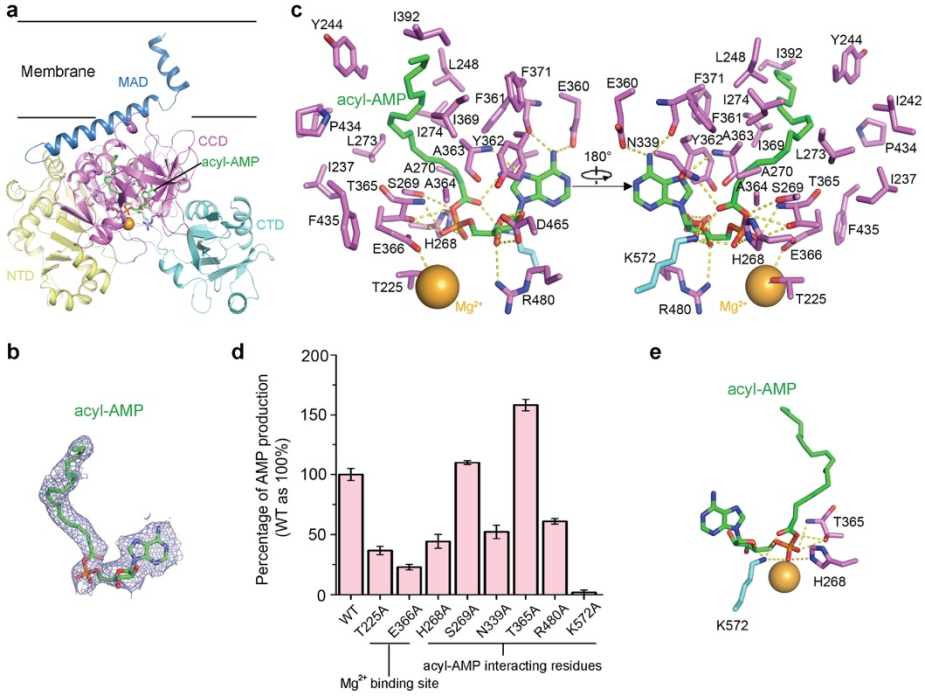

Fig. 3 The acyl-AMP and Mg^{2+} binding sites. a, Binding between the acyl-AMP and FATP2. **b,** The cryo-EM density of the acyl-AMP. **c,** Interaction details at the acyl-AMP and Mg^{2+} binding sites. **d,** Relative AMP generation by FATP2 mutants at binding sites of Mg^{2+} and the acyl-AMP. AMP production of WT FATP2 was taken as 100%. **e,** Interactions between His268, Lys572, Thr365 and the acyl-AMP.

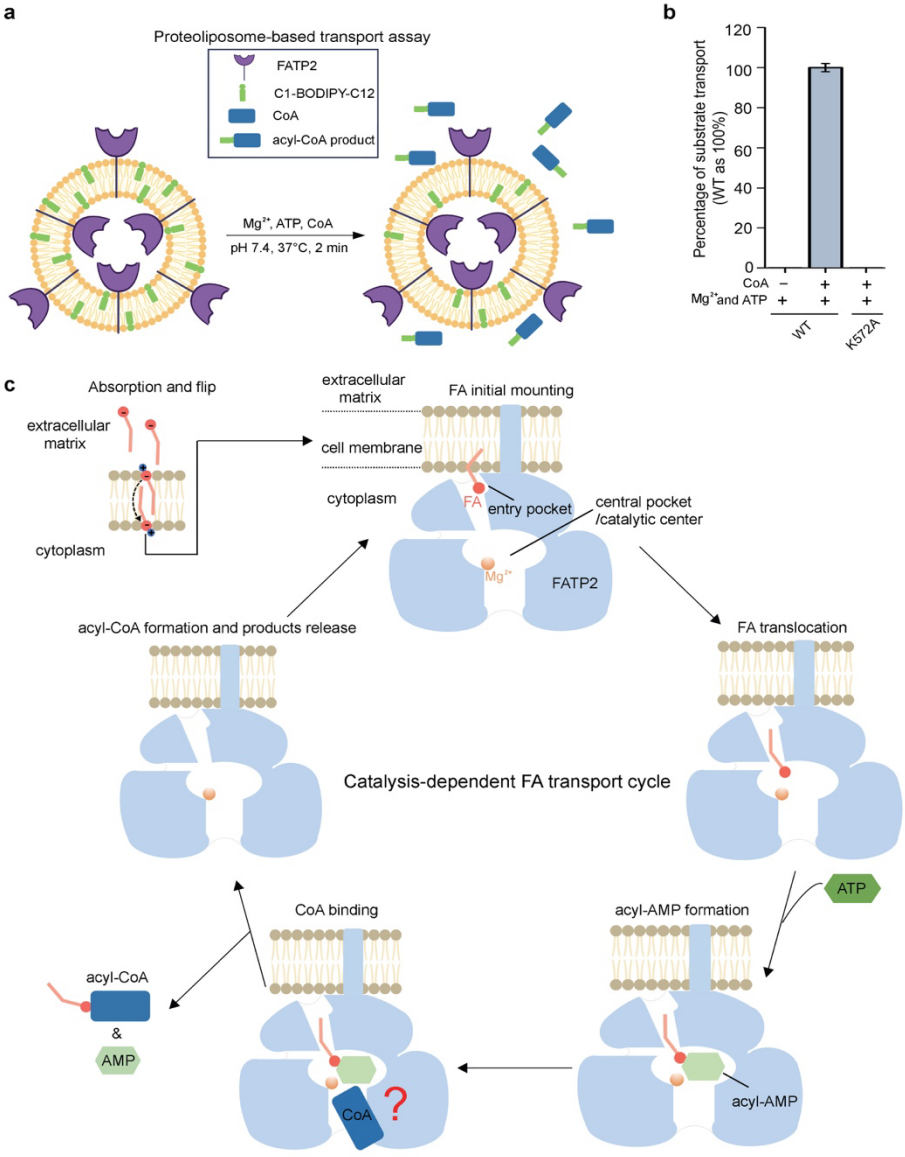

458

459 **Fig. 4 Mechanism of FATP2-mediated FA transport. a,** A proteoliposome-based assay for the
460 measurement of FA transport. The fluorescence-labeled FA derivative C1-BODIPY-C12 was used as
461 the FA substrate and incorporated into the proteoliposomes. The C1-BODIPY-C12 molecules in the
462 lipid bilayer were transported by the outward-oriented FATP2 towards external environment. Mg^{2+},
463 ATP and CoA was supplemented into the external buffer at pH 7.4 and lasted for 2 min at 37°C for
464 reaction. Liposomes were removed through centrifugation and fluorescence of supernatants were
465 recorded. **b,** Relative substrate transport of FATP2 variants with or without the presence of CoA. The
466 fluorescence of the sample of WT FATP2 with Mg^{2+}, ATP and CoA supplemented was recorded and
467 taken as 100%. Data are shown as mean ± s.d., n = 3 technical replicates. Experiments were
468 independently repeated twice. **c,** A working model of FATP2. FA absorbed by membrane is first
469 mounted to FATP2 at the entry pocket, followed by translocation to the central pocket and gain
470 access to the catalytic center for the generation of acyl-AMP in the presence of ATP. CoA binds to
471 FATP2 with its thiol group reaching to the reaction center for the acceptance of the acyl-group from
472 acyl-AMP. The final products acyl-CoA and AMP will be released into cytoplasm. A new FA substrate
473 may be extracted from the membrane and mounted into the entry pocket as long as it is empty.

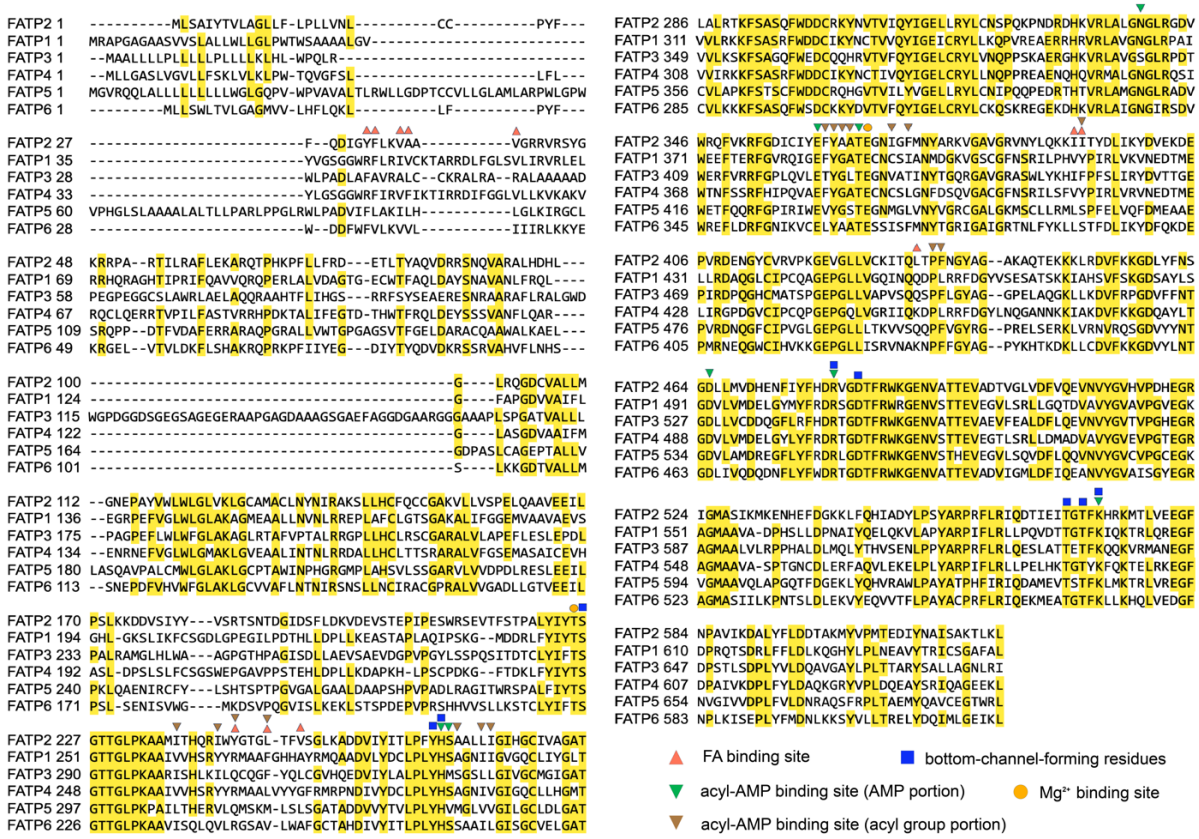

Supplementary Figure. 1 | Sequence alignment between human FATP1-6. Sequences of human FATP1-6 with UniProt codes of Q6PCB7, O14975, Q5K4L6, Q6P1M0, Q9Y2P5 and Q9Y2P4 are aligned using SnapGene. Identical residues at corresponding positions are highlighted with yellow background. Residues that form the FA binding site, AMP and acyl group portions of the acyl-AMP binding site, Mg^{2+} binding site and the bottom channel in the cryo-EM structure of FATP2 are indicated by corresponding symbols as illustrated in the figure.

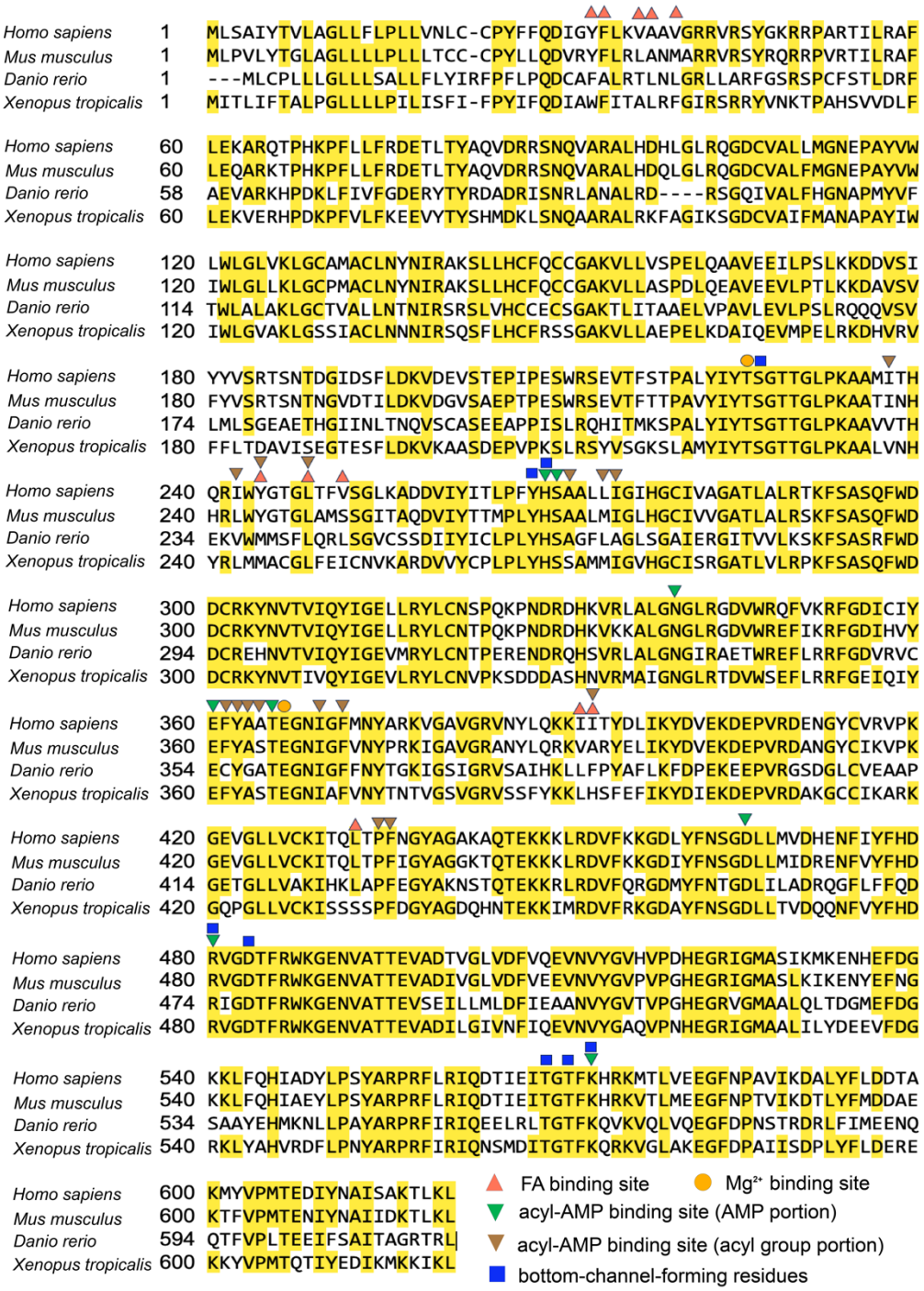

Supplementary Figure. 2 | Sequence alignment between FATP2s from different species. Sequences of FATP2s from Homo sapiens (UniProt code: O14975), Mus musculus (UniProt code: O35488), Danio rerio (UniProt code: Q4KMC7) and Xenopus tropicalis (UniProt code: A0A8J0QWD8) are aligned using SnapGene. Identical residues at corresponding positions are highlighted with yellow background. Residues that form the FA binding site, AMP and acyl group portions of the acyl-AMP binding site, Mg^{2+} binding site and the bottom channel in the cryo-EM structure of FATP2 are indicated by corresponding symbols as illustrated in the figure.

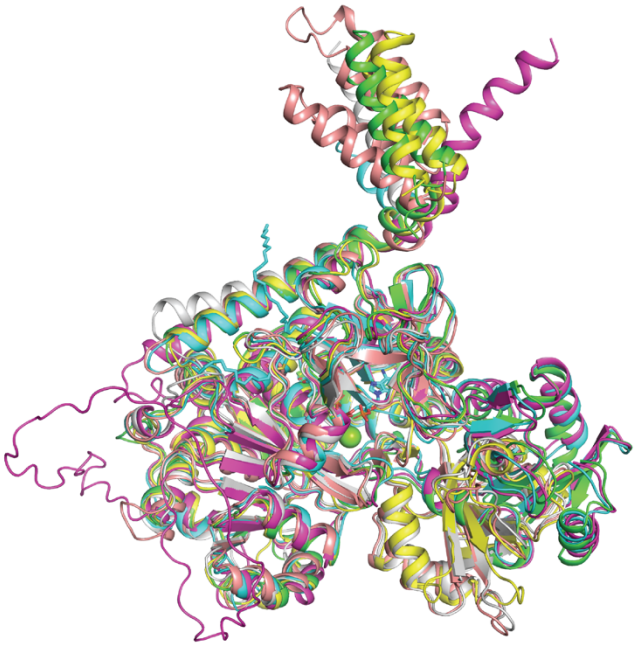

Supplementary Figure. 3 | Structural alignment between cryo-EM structure of FATP2 and Alphafold-predicted structures of rest human FATPs. Structures of human FATP1-6 are colored in green, cyan, magenta, yellow, salmon and grey, respectively.